Thermal Conductivity of Snow on Arctic Sea Ice

Amy R. Macfarlane[1], Henning Löwe[1], Lucille Gimenes[1], David N. Wagner[1,2], Ruzica Dadic[1,3],
Rafael Ottersberg[1], Stefan Hämmerle[4], and Martin Schneebeli[1]

[1]WSL Institute for Snow and Avalanche Research SLF, Davos Dorf, Switzerland
[2]CRYOS, School of Architecture, Civil and Environmental Engineering, EPFL, Lausanne, Switzerland
[3]University of Wellington, Wellington, New Zealand
[4]Scanco Medical AG, Bassersdorf, Switzerland

Correspondence: Amy R. Macfarlane (amyrmacfarlane@gmail.com)

Abstract.

Snow significantly impacts the seasonal growth of Arctic sea ice due to its thermally insulating properties. Various measurements and parametrizations of thermal properties exist, but an assessment of the entire seasonal evolution of thermal conductivity and snow resistance is hitherto lacking. Using the comprehensive snow data set from the MOSAiC expedition, we have evaluated for the first time the seasonal evolution of the snow's thermal conductivity and thermal resistance on different ice ages (leads, first and second-year ice) and topographic features (ridges). Combining different measurement parametrizations and assessing the robustness against spatial variability, we infer and quantify a hitherto undocumented feature in the seasonal dynamics of snow on sea ice. We observe an increase in thermal conductivity up to March and a decrease thereafter, both on first-year and second-year ice before the melt period started. Since a similar non-monotonic behaviour is extracted for the snow depth, the thermal resistance of snow on level sea ice remains approximately constant with a value of 515 ± 404 $\mathrm{m}^2\,\mathrm{K}\,\mathrm{W}^{-1}$ on first-year ice and $660 \pm 475\,\mathrm{m}^2\,\mathrm{K}\,\mathrm{W}^{-1}$ on second-year ice. We found approximately three times higher thermal resistance on ridges ($1411 \pm 910\,\mathrm{m}^2\,\mathrm{K}\,\mathrm{W}^{-1}$). Our findings are that the micropenetrometer-derived thermal conductivities give accurate values, and confirm that spatial variability of the snow cover is vertically and horizontally large. The implications of our findings for Arctic sea ice are discussed.

1 Introduction

Snow's thermal conductivity and insulating properties directly impact heat transfer through the ice and directly inhibit ice growth in the winter season (Sturm and Massom, 2017). Due to this, snow accumulation and snow stratigraphy in winter directly influence the mass balance and, consequentially the energy balance of sea ice (Eicken et al., 1995; Fichefet and Maqueda, 1997; Sturm et al., 2002). The snow cover is often stated as the dominant uncertainty in estimates of sea ice thickness, largely because of its high variability in this landscape, realized from laboratory and in situ field measurements (Sturm et al., 2002). Variability of snow's thermal conductivity stems from the texture, e.g., specific surface area, anisotropy, connectivity and density (Mellor, 1977; Sturm et al., 1997, 2002). Understanding this relationship and heterogeneity requires detailed and numerous microstructural measurements of snow on Arctic sea ice. The lack of these, due to the inaccessibility of this area in the winter season and shortfalls in the methods (Riche and Schneebeli, 2013), has limited research on the spatial and temporal variability of heat transfer through the snow. Consequentially, accurately calculating the energy balance variability of sea ice in the high Arctic has considerable shortcomings (West et al., 2020).

There are three potential processes of heat transfer through the snow: 1) conduction through the ice skeleton, 2) conduction, convection, and radiation across air spaces, and 3) vapour diffusion between the snow grains (Yen et al., 1991). Conduction across the air spaces and radiation heat transfer is negligible (Sturm et al., 2002). Convection and vapour diffusion depend on the permeability and hence the ice volume fraction of the snow. Due to this, the high ice volume fraction of snow wind slabs on sea ice reduces convection and vapour diffusion. This results in conduction through the ice skeleton being the foremost process influencing heat transfer through the snow cover.

X-ray micro-computed tomography (microCT) has enabled snow research to advance by measuring the exact ice skeleton without damaging it (Riche and Schneebeli, 2010), which allows calculations of the microstructure's textural properties. Direct numerical simulations of heat conduction through the ice skeleton and the pore space using the finite element method (FEM) (Arns et al., 2001; Kaempfer et al., 2005; Petrasch et al., 2008; Calonne et al., 2011) is currently the most reliable method to measure the thermal conductivity of snow (Riche and Schneebeli, 2013). This opens new opportunities to investigate the relationship between textural properties and heat transport.

Density is currently used to parametrize thermal conductivity because it is a simple, low cost and quick measurement in the field (Orvig, 1970; Yen, 1981; Fukusako, 1990; Radionov et al., 1997; Sturm et al., 1997; Warren et al., 1999; Sturm et al., 2002; Domine et al., 2011; King et al., 2020; Arndt, 2022). However, we are now aware of shortfalls when excluding other necessary textural properties from thermal conductivity parametrizations. Löwe et al. (2013) highlights that the samples' anisotropy plays a significant role in the heat transfer through the snowpack and presents a parametrization for thermal conductivity using density and anisotropy for snow (specifically for densities below $500 \ \mathrm{kg \, m^{-3}}$). However, this parametrization is not adapted to high snow densities. Pitman and Zuckerman (1967); Fukusako (1990); Singh (1999); Smith and Jamieson (2014); Calonne et al. (2019) realized the influence of temperature on a snow microstructure's thermal conductivity. Calonne et al. (2019) created upper bounds to ensure that in the higher density ranges, the thermal conductivity is in agreement with the thermal conductivity of ice at specific temperatures. However, their parametrization does not include anisotropy. In summary, very few

thermal conductivity measurements are simulated from the high Arctic (Gouttevin et al., 2018); therefore, the influence of anisotropy is unknown.

Spatial heterogeneity of the snow on sea ice requires a very high number of measurements, which can not only be realized by microCT. A faster method is needed. We used high-resolution penetrometry using a SnowMicroPen to improve spatial coverage. Sturm et al. (2002) and King et al. (2020) studied the spatial heterogeneity of snow on Arctic sea ice; however, very few studies have investigated temporal changes, in contrast to the snow on Arctic tundra (Domine et al., 2016; Sturm and Johnson, 1992). Thermal conductivity measured from thermistor strings installed in the snow and ice (Huwald et al., 2005; Pringle et al., 2007; Marchenko et al., 2019) measures temporal changes in thermal conductivity. They are also destructive measurements and disturb the snow cover during and after installation. Therefore it is challenging to accurately capture the snow's effective thermal conductivity using this method.

Given the importance of snow in the sea ice system, we work towards advancing our understanding of both spatial and temporal heterogeneity of the thermal conductivity of snow on sea ice in the high Arctic. We present two new parametrizations, with and without anisotropy for the complete range of possible snow/firn densities, developed using the microCT FEM method using snow samples collected during the MOSAiC expedition (Section 2.1). We up-scaled individual microCT profiles (Section 2.2) by using snow micro penetrometer density profiles (Section 2.3) to identify both spatial and temporal trends in the data set (Section 3.3). Our measurement concept considered the spatial heterogeneity of sea ice (Nicolaus et al., 2022), and as a result, we could draw previously impossible conclusions about the thermal conductivity and resistance of the snow cover on different ice types over the entire winter. This is relevant for calculating the Arctic sea ice's energy budget and allows us to better understand sea ice growth in the winter. We finally compare our data set to the average snow thermal conductivity value of $0.32 \pm 0.01 \, \mathrm{W \, K^{-1} \, m^{-1}}$, used in the modelling community (Sturm et al., 2002; Lecomte et al., 2013; Holland et al., 2021).

2 Data and methods

2.1 MOSAiC expedition

Field measurements used in this study were conducted as part of the MOSAiC expedition in the winter months from November 2019 to May 2020. The field measurements were located on drifting Arctic sea ice, with the first measurement at 85^o79'N 123^o00'S, reaching a maximum latitude of 88^o56'N 45^o53'S and then drifting South until 83^o42'N 12^o67'S. A single ice floe was studied in this period. To understand the snow conditions, we set up snowpit sites on the sea ice, where we took weekly measurements. These were marked with flags so we could relocate the same snowpit site on the next visit and create time series of measurements at that location. The snowpit sites were randomly distributed across the ice floe to sample different ice types (e.g. first-year ice (FYI), second-year ice (SYI) and leads) and topographic features (e.g. ridges). However, the exact location cannot be sampled twice due to the destructive nature of most measurements within the snowpit. To continue a time series at one snowpit site, the snowpit operator measured consecutive snowpits approximately 1 meter apart. Locations of each snowpit site are indicated alongside the data set paper (Macfarlane et al., 2021b). A snowpit is a collection of measurements measuring the physical properties of the snowpack at the same snowpit site at one point in time. The snowpit analysis used in this study

focused on the physical properties of the snowpack, including depth, density, anisotropy and thermal conductivity. In this study, we focus on the MOSAiC snowpit data set (Macfarlane et al., 2021b), of which three key instruments were the focus of this study. The instruments included a i) microCT, ii) SMP, and iii) density cutter. Details of these instruments are given in sections 85 2.2, 2.3 and 2.4.

2.2 MicroCT Samples

The data set evaluated for this manuscript includes 138 microCT samples (approximately 10 cm high and 6.6 to 7.8 cm diameter) collected during 69 individual trips to the sea ice, known as 'Events'. More than one microCT sample was often collected during an event to sample the complete snow profile. An overview of the samples taken at specific dates and their 90 heights can be seen in Fig. 1. The EventID (a unique labelling system representing one trip to the ice) can be used to identify co-located microCT samples. The snow samples were extracted using a cylindrical drill, carefully placed in a sample holder and transported back to the laboratory on board *Polarstern* (Knust, 2017). By installing a desktop cone-beam microCT90 in a laboratory onboard, we could measure the microstructure of the snow semi-in situ. The laboratory was cooled to $-15\,^oC$, and the microCT had a custom ventilation system meaning the sample remained at $-12\,^oC$ during the scanning process. Once 95 the snow samples were scanned, the data was analyzed by dividing each snow sample into sub-samples of volume 5.83 cm^3 to calculate the density, the geometrical anisotropy $A_g = 2\xi_z/(\xi_x + \xi_y)$ from the correlation lengths ξ in different coordinate directions (Löwe et al., 2013) and the effective thermal conductivity using FEM.

2.2.1 Direct numerical simulations using FEM, $k_{\mathrm{eff}}^{\mathrm{FEM}}$

MicroCT samples and the FEM were used to obtain effective thermal conductivity of the snow. The effective thermal conductiv- 100 ity (k_{eff}) characterizes the steady-state heat flow through a unit area of a homogeneous material induced by a unit temperature gradient in a direction perpendicular to that unit area (W K^{-1} m^{-1}). The relationship is shown in Equation (1), where h is the sample thickness (m), T represents the temperature (K), and q represents the volume averaged heat flux (W m^{-2}).

$$k_{\mathrm{eff}} = q\frac{h}{\Delta T} \tag{1}$$

The simulated thermal conductivities k_{eff} can be used to characterize the thermal anisotropy A_k of the samples in the x, y 105 and z direction, as seen in Equation (2).

$$A_k = \frac{2k_{\mathrm{eff}(z)}}{k_{\mathrm{eff}(x)} + k_{\mathrm{eff}(y)}}, \tag{2}$$

The thermal conductivity of the microCT sub-samples, calculated using the FEM method ($k_{\mathrm{eff}}^{\mathrm{FEM}}$), were compared to the density and A$_k$ of the sub-samples, seen in Fig. 2 to identify sources of variability. The numerical simulation uses the code from Garboczi et al. (1998) and precisely follows the procedures described by Löwe et al. (2013); Gouttevin et al. (2018). For 110 the thermal conductivity of ice and air, we used their values at $T = -20\,^oC$, namely $k_{\mathrm{ice}} = 2.34$ W K^{-1} m^{-1}, (Slack, 1980) and $k_{\mathrm{air}} = 0.024$ W K^{-1} m^{-1}. Based on the simulated heat flux and the prescribed temperature gradient, $k_{\mathrm{eff}}^{\mathrm{FEM}}$ is calculated using Equation (1).
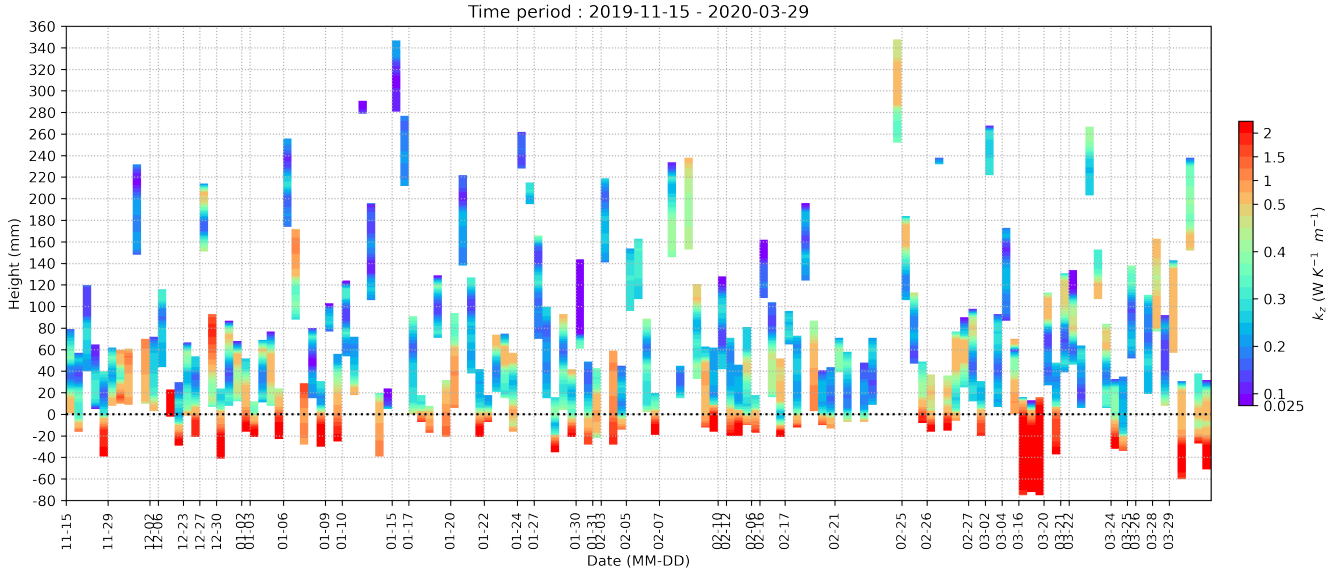
Figure 1. Samples of effective thermal conductivity plotted against time. Samples of snow were collected during the winter period to be measured using micro-computed tomography. We could simulate effective thermal conductivity across these samples using the FEM method. Here we see each sample plotted at the height taken in the snowpack against the collection date. Negative heights correspond to samples of the sea ice beneath the snowpack. This figure highlights the vertical variability within the samples.

2.2.2 Parametrizations of thermal conductivity, $k_{\text{eff}}^{\text{X}}$

X in $k_{\text{eff}}^{\text{X}}$ represents the different parametrizations of thermal conductivity. $k_{\text{eff}}^{\text{X}}$ parametrizations tested in this study used a) density from Yen (1981); Sturm et al. (2002), where X = Yen, Stm respectively, b) density and temperature from Calonne et al. (2019), where X = Cal3, Cal20, Cal60 for different temperature parametrizations, and c) density and A_k from Löwe et al. (2013), where X = Löwe. By comparing these parametrizations to the values of $k_{\text{eff}}^{\text{FEM}}$ we could identify which parameters are optimal for measuring $k_{\text{eff}}^{\text{X}}$ for snow on Arctic sea ice. After conducting this analysis, we calculated the second-order polynomial fit for this data set to obtain a density parametrization specific for snow on sea ice, as seen in Equation (3), where ρ represents the density of the sub-samples, $a = 2.62 \times 10^{-6}$, $b = 1.54 \times 10^{-33}$ and $c = 3.04 \times 10^{-2}$

$$k_{\text{eff}}^{\text{Mac(I)}} = a\rho^2 + b\rho + c \tag{3}$$

When allowing for anisotropy in the parametrization, it is straightforward to generalize the empirical correction of Löwe et al. (2013) to obtain an accurate parametrization as a function of density and A_g in the entire density range. To this end, we use the empirical transformation as a function of the lower bound values $k^{(\text{L})}$ which were calculated from Eq. 2 in (Löwe et al., 2013) through density and A_g. Here Ω, β, k_0 are adjustable parameters which are obtained by minimizing the differences
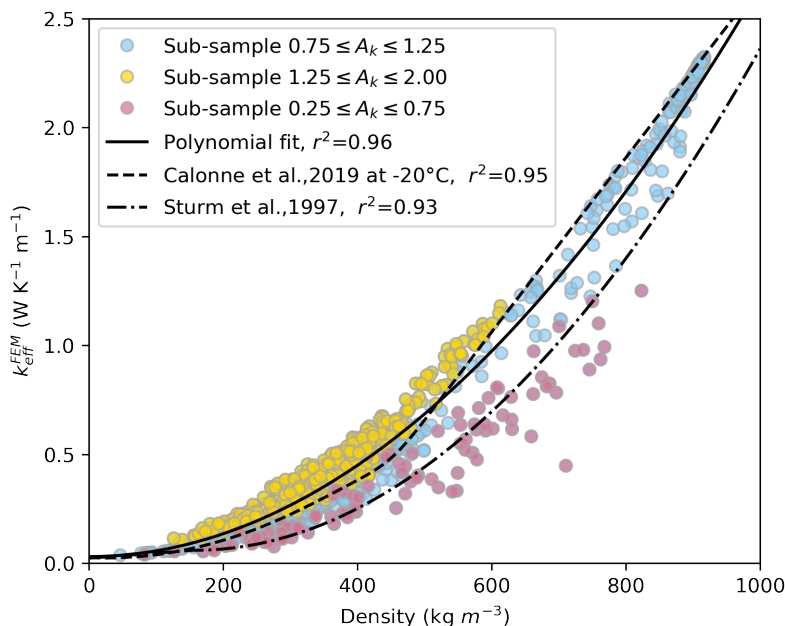
Figure 2. The sub-sample's density plotted against effective thermal conductivity, the colour indicates an anisotropy range. Direct numerical simulations of the effective thermal conductivity using the finite element method (FEM) for the sub-samples are compared to the sub-sample density. A polynomial fit of the data is shown in the solid line. This relationship between effective thermal conductivity and density has been tested in previous studies. This figure includes two current parametrizations (Calonne et al., 2019; Sturm et al., 1997). Anisotropy values are indicated in different colours with details given in the legend and the figure shows how anisotropy influences the effective thermal conductivity of the sub-samples.

between Equation (4) and the FEM estimates.

$$k_{\text{eff}}^{\text{Mac(II)}} = k_0 + \left(\frac{k^{(\text{L})\beta}}{\Omega(1 - k^{(\text{L})}) + k^{(\text{L})(\beta-1)}} \right) \tag{4}$$

2.3 SMP profiles

The SMP evaluated the penetration force resistance of a snow profile at 0.3 mm vertical resolution. Five SMP force profiles
130   were obtained within one snowpit, approximately 0.25 meters apart. Additional measurements were often taken on both sides of the snowpit to capture the spatial variability of the snow in the surrounding area. These additional SMP measurements were taken at intervals of one meter. This reduced operator bias when selecting an area to measure. Further details can be found alongside the published SMP data Macfarlane et al. (2021a) set within the snowpit bundle (Macfarlane et al., 2021b). 3266 SMP profiles are used in this study. The SMP penetration force profile can be used to obtain density and, in combination with
135   parametrizations listed in the previous section, estimates of the thermal conductivity. We used the density parametrization from

King et al. (2020) after testing a few profiles against the density obtained from the microCT. We found that this parametrization was optimal, likely because the King et al. (2020) SMP data set was also collected on sea ice in the high Arctic.

2.3.1 The effective thermal conductivity's harmonic mean, $\overline{k_{\text{eff}}^{\text{X}}}$

The thermal gradient in a snowpack is vertical. For a layered material, such as snow, the average thermal conductivity is

140 represented in analogy to Ohm's law by conduction resistances in series (Bergman et al., 2011). In our case, as all sub-samples have the same dimension, this simplifies the harmonic mean. The harmonic mean of a snow profile's thermal resistance ($\overline{k_{\text{eff}}^{\text{X}}}$) is calculated using Equation (5). Where n is the number of sub-samples in a profile, and k_i is the effective thermal conductivity of individual sub-samples, as all sub-samples have the same dimension.

$$\overline{k_{\text{eff}}^{\text{X}}} = \left(\frac{\sum\limits_{i=1}^{n} k_i^{-1}}{n} \right)^{-1} \tag{5}$$

145 After testing the current literature's k_{eff} parametrizations, we used the parametrization with the highest r² in relation to this dataset to upscale the single snowpits. The harmonically averaged $\overline{k_{\text{eff}}^{\text{X}}}$ of all the SMP profiles in winter were then grouped depending on the snowpit site's underlying ice type (e.g. FYI areas, SYI areas, or leads), topographic features (e.g. ridges), and month to better understand spatial variability.

2.3.2 Average effective thermal Resistance, R

150 The SMP measurements of thermal conductivity and snow depth were used to investigate the snow's thermal resistance (R) on the ice floe using the $k_{\text{eff}}^{\text{Mac(I)}}$ parametrization. The snowpack's R-value is the temperature difference, at steady state, between the ice-snow interface and ice-atmosphere interface, given a unit heat flow rate through a unit area ($\text{m}^2\,\text{K}\,\text{W}^{-1}$). By combining this definition and Equation (1), the snowpack's R can be found by dividing the snow depth (HS) by the profile's $\overline{k_{\text{eff}}^{\text{X}}}$, as seen in Equation (6).

155 $$R = \frac{\Delta T}{q} = \frac{\text{HS}}{\overline{k_{\text{eff}}^{\text{X}}}} \tag{6}$$

The measurements were grouped as mentioned in Section 2.3.1.

2.4 Density profiles

We further investigated the reduction in density in April and May by using all density measurements available. The instruments that are used to measure density include a density cutter (ρ^{Cutter}), a SWE tube (ρ^{SWE})and the SMP measurements (ρ^{SMP}).

160 ### 2.5 Atmospheric data

Due to a reduction of density during this period using three independent instruments, we further used shortwave radiation data (Riihimaki, 2021) from up and down radiometer systems, temperature and wind data measured at 2 m (Cox et al., 2021) from a

meteorological flux tower. These instruments were deployed at Met City (a station approximately 200 m away from the snowpit measurements). This additional atmospheric data helped us understand and explain the conditions that might have caused the

165 density reduction.

3 Results

3.1 Direct numerical simulations using FEM, $k_{\mathrm{eff}}^{\mathrm{FEM}}$

Individual vertical snow profiles showed high-density variability, $k_{\mathrm{eff}}^{\mathrm{FEM}}$ and A_k. Icy layers within the snow profile, crusts on the surface and a 'remnant surface scattering layer' at the snow-ice interface (a granular layer at the top of the melting summer

170 sea ice (Perovich et al., 1996)) were of high density, in contrast to the low-density fresh snow. The vertical profiles of $k_{\mathrm{eff}}^{\mathrm{FEM}}$ in Fig. 1 highlight the large variability amongst samples, showing that snow stratigraphy highly influences thermal conductivity. The commonly occurring layers of depth hoar and rounded, wind-blown snow are of similar densities of approximately 300 kg m^{-3}. Due to these two grain types being dominant on Arctic sea ice, we see a large proportion of our sub-sample's densities in the range of 200 to 400 kg m^{-3}, seen in the high point concentration in this density range in Fig. 2. The variability and different

175 colours in this figure show the range of A_k values and the influence of A_k on $k_{\mathrm{eff}}^{\mathrm{FEM}}$. A_k values ranged between 0.25 and 2, indicated in the legend in Fig. 2. The density distribution of the $k_{\mathrm{eff}}^{\mathrm{FEM}}$ values are shown in Fig. 3, after a 550 kg m^{-3} density cut-off is applied to exclude ice samples (Blunier and Schwander, 2000). The average $k_{\mathrm{eff}}^{\mathrm{FEM}}$ value is 0.27 ± 0.17 W K^{-1} m^{-1}. The errors given throughout this manuscript are one standard deviation ($\pm\, 1\sigma$).
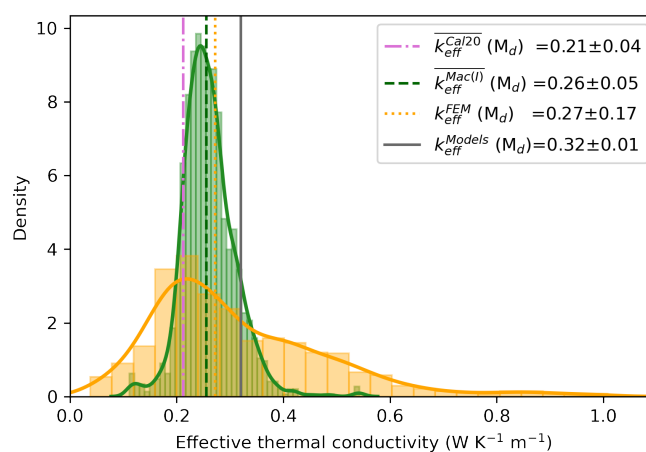
Figure 3. Density plot of effective thermal conductivity. This plot shows the density distribution of $k_{\mathrm{eff}}^{\mathrm{FEM}}$ for all microCT sub-samples with densities below 550 kg m^{-3} and the harmonic mean of the SMP profiles ($\overline{k_{\mathrm{eff}}^{\mathrm{Mac(I)}}}$) from January to March 2020. The median values are indicated with the symbol M$_d$ in the legend. The error given in the legend represents one standard deviation.

3.2 Parametrizations of thermal conductivity, $k_{\text{eff}}^{\text{X}}$

180 The high variability amongst samples allowed our data set to cover all possible density and anisotropy values, allowing us to test each $k_{\text{eff}}^{\text{X}}$ parametrization currently presented in this field.

When comparing $k_{\text{eff}}^{\text{X}}$ to $k_{\text{eff}}^{\text{FEM}}$ for all sub-samples, Fig. 4 shows the relationship for current parametrizations for the full range of possible snow densities. The r^2 values for each parametrization can be found in Fig. 4. Using the parametrization $k_{\text{eff}}^{\text{Löwe}}$ results in a low r^2 value since in the original work (Löwe et al., 2013) the adjustable coefficients were optimized only in

185 the density range below 500 kg m^{-3}). Adapting the work from (Löwe et al., 2013) using 4 results in a correlation coefficient of $r^2 = 0.99$. This $k_{\text{eff}}^{\text{Mac(II)}}$ relationship to $k_{\text{eff}}^{\text{FEM}}$ is shown in Fig. 4.
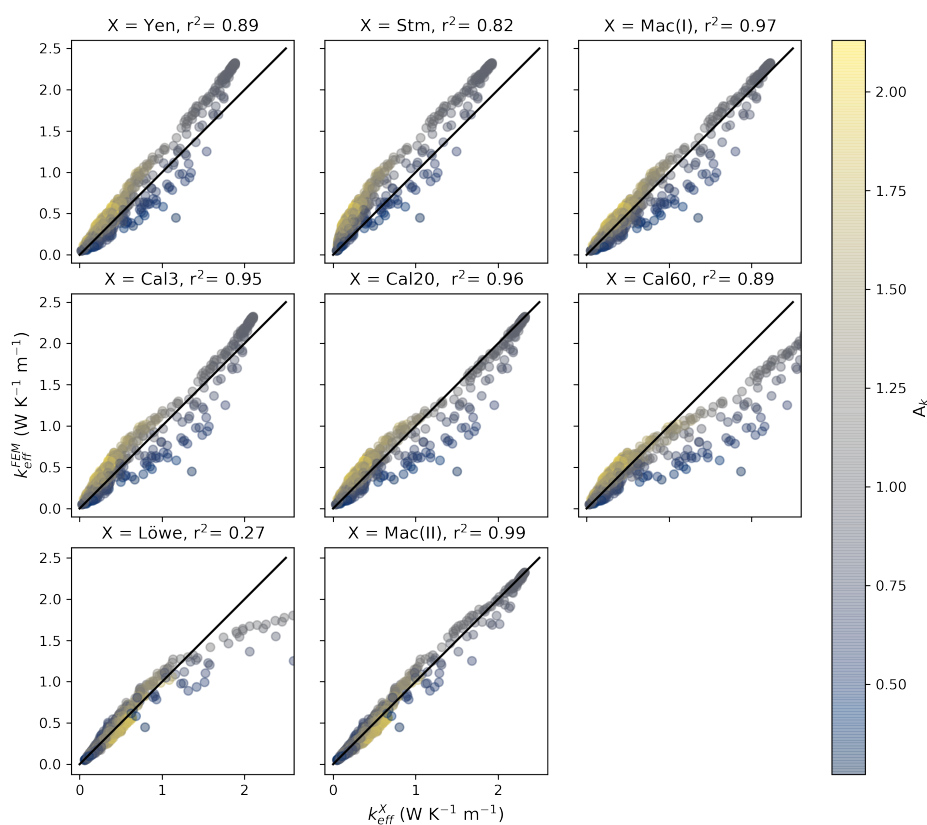
Figure 4. Different parametrizations of effective thermal conductivity plotted against effective thermal conductivity measured using the FEM method. Each sub-sample was used to measure effective thermal conductivity using i) direct numerical simulations on a finite element method (FEM), and ii) different parametrizations using density, anisotropy and temperature. The top row shows the performance of density parametrizations (Yen (1981); Sturm et al. (1997). The polynomial fit of this data set, $k_{\text{eff}}^{\text{Mac(I)}}$), the middle row shows the performance of density and temperature parametrizations from Calonne et al. (2019) for -3°C, -20°C and -60°C. The bottom row shows parametrizations using anisotropy (Löwe et al., 2013) and the new parametrization as an outcome of this study ($k_{\text{eff}}^{\text{Mac(II)}}$).

Ice type	HS (mm)	ρ^{SMP} (kg m^{-3})	$\overline{k_{\mathrm{eff}}^{\mathrm{Mac(I)}}}$ (W K^{-1} m^{-1})	R (m^2 K W^{-1})
Leads	84 ± 124	301 ± 41	0.25 ± 0.06	350 ± 469
FYI	129 ± 109	294 ± 32	0.24 ± 0.05	515 ± 404
SYI	144 ± 113	277 ± 26	0.22 ± 0.04	660 ± 475
Ridges	335 ± 278	304 ± 30	0.26 ± 0.05	1411 ± 910

Table 1. The median ($\pm 1\ \sigma$) of snow depth (HS), density (ρ^{SMP}), harmonically averaged effective thermal conductivity using the Mac(I) parametrization ($\overline{k_{\mathrm{eff}}^{\mathrm{Mac(I)}}}$), and thermal resistance (R) for each ice type.

Without including anisotropy in the parameterization, $k_{\mathrm{eff}}^{\mathrm{Mac(I)}}$ is the best representation of k_{eff}, as it has the highest r^2 value compared to this dataset. We use this parametrization and introduce the SMP to upscale our measurements of k_{eff}, of which we do not have corresponding A$_k$ or A$_g$ measurements.

190   The harmonic mean reduces any profile outliers, the $\overline{k_{\mathrm{eff}}^{\mathrm{X}}}$ profiles therefore have a smaller range of values in the histogram in Fig. 3. Despite the reduction in the range, the median value of $\overline{k_{\mathrm{eff}}^{\mathrm{Mac(I)}}}$ (M$_d = 0.25 \pm 0.05$ W K^{-1} m^{-1}) aligns with the median value of $k_{\mathrm{eff}}^{\mathrm{FEM}}$. For the rest of the study, we use SMP profiles and the effective thermal conductivity's harmonic mean, $\overline{k_{\mathrm{eff}}^{\mathrm{Mac(I)}}}$, using the density of the SMP profiles (ρ^{SMP}) calculated using King et al. (2020) parametrization of density to investigate spatial heterogeneity and temporal changes of the snow cover on Arctic sea ice.

195 **3.3 Spatial heterogeneity and temporal changes**

To understand the heterogeneity of the snow depth (HS), we categorized the snowpits into ice type and ridged areas, seen in the grey box plots in Fig. 5. Table 1 gives the median and standard deviation of each. Looking at individual months in the coloured bar charts (displayed in Fig. 5) shows snow depth is highly variable on SYI. On FYI, we see an increase in snow depth until March and then a decrease. We also see more outliers in the FYI data set. Leads and ridges show consistently high spatial

200 heterogeneity; therefore, any temporal changes are less discernible than FYI and SYI areas.

The snow density (ρ^{SMP}) median is slightly higher on leads, FYI and ridges, compared to snow densities on SYI (values are given in Table 1). Snow density has a similar monthly trend on all ice types (shown in the coloured boxplots in Fig. 5), increasing until March and then decreasing in April and May. Looking at the median density values for this season in Fig. 6 shows this feature in multiple data sets, not just the SMP. To better understand the reason for this density decrease, the SMP

205 penetration resistance was normalized for the snow depth to see changes throughout the season. This can be seen in Fig. 7. This figure shows a penetration force reduction in May at the surface and lower depths of the snow cover. This is further discussed in Section 4.3.
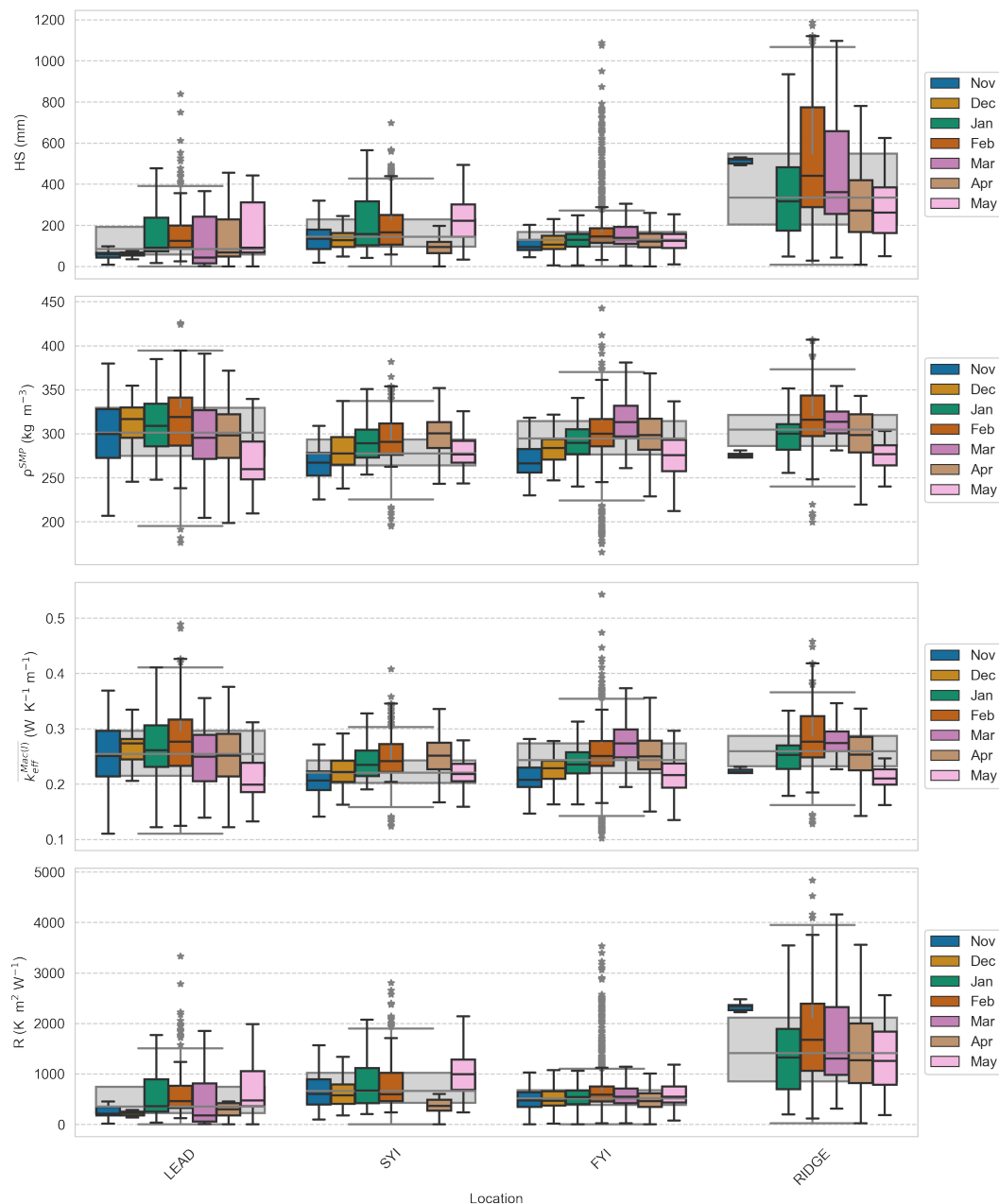
Figure 5. Snow depth (HS)**, density** (ρ^{SMP})**, harmonically averaged thermal conductivity** ($\overline{k_{\mathrm{eff}}^{\mathrm{Mac(I)}}}$) **and resistance (R) were all measured using a snow micro-penetrometer and plotted against underlying ice type and month.** A snow micro penetrometer was used to measure vertical profiles of penetration resistance. These profiles can be used to extract snow depth, density (using King et al. (2020)), harmonically averaged effective thermal conductivity using the Mac(I) parametrization, given in Equation (3), with the King et al. (2020) derived density as an input, and finally the resistance of the snowpack (R). These profiles are grouped by underlying ice type, topographic feature (seen in the grey bar charts), and month (seen in the coloured bar charts).
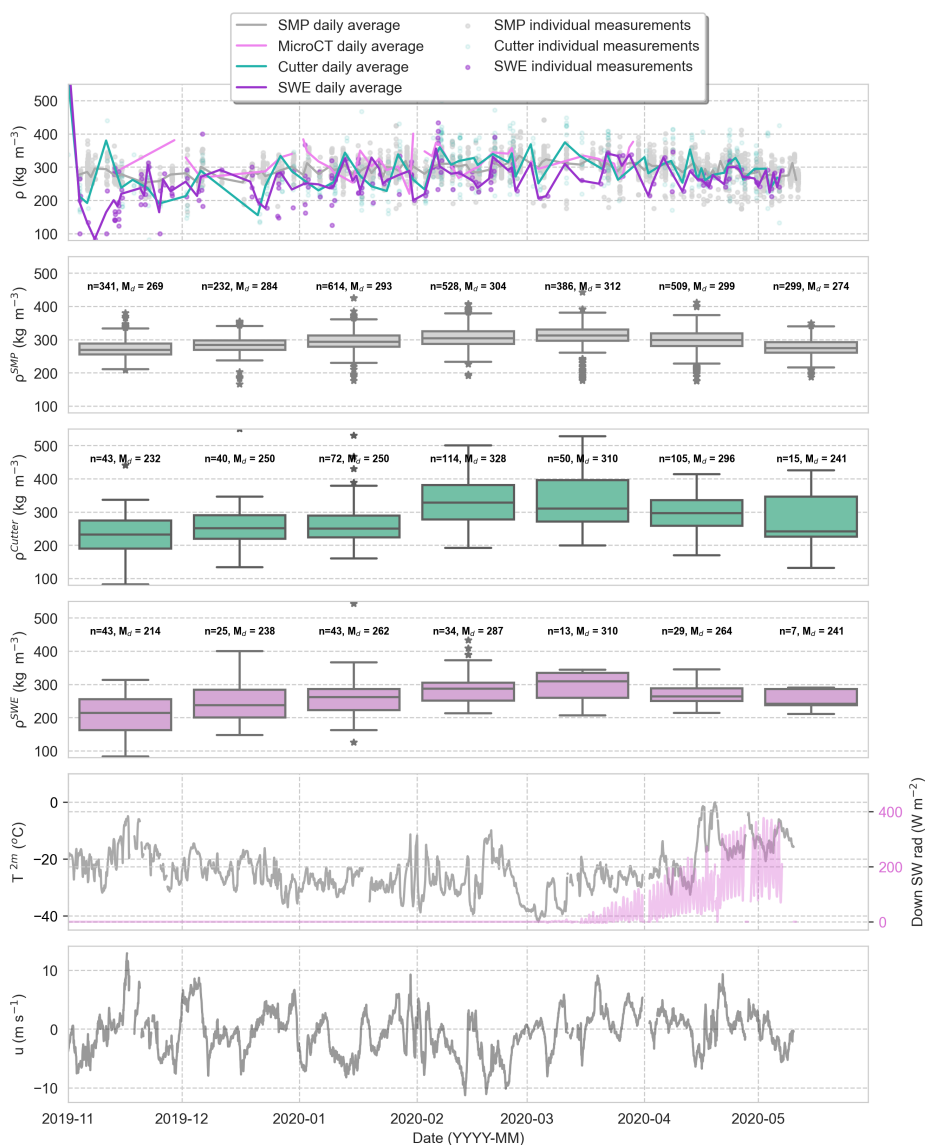
Figure 6. Timeseries of density using three independent instruments, the air temperature at 2 meters (T^{2m}), downward shortwave (SW) radiation and wind speeds (u). Density measurements from different instruments within the snowpit are compared in the upper plot against time. This emphasizes the variability amongst different instruments and the spatial variability of the snow density over the ice floe. Box plots of the same density measurements show the temporal change in the medians (M_d). n is the number of data points in each box plot. We attempt to explain the decrease in densities after March using atmospheric measurements from a nearby tower. The temperature two meters above the snow surface, the downward shortwave radiation and the wind speed are plotted simultaneously as the density measurements for this comparison.
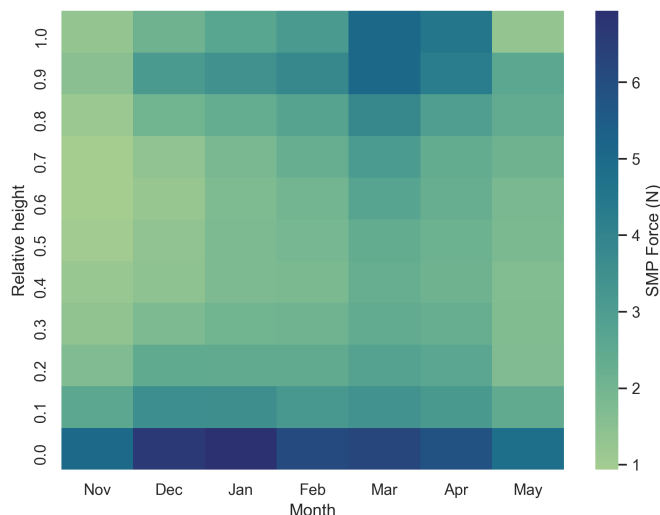
Figure 7. A heatmap of snow micro-penetrometer profiles throughout the winter season on level FYI and SYI. All snow micro penetrometer profiles are concatenated, and their depths are normalized. The average SMP force signals for all profiles within one month are displayed throughout the winter to show seasonal changes in the snow cover.

$\overline{k_{\mathrm{eff}}^{\mathrm{Mac(I)}}}$ has a slightly lower median on FYI and SYI, compared to leads and ridges with a higher $\overline{k_{\mathrm{eff}}^{\mathrm{Mac(I)}}}$, seen in Table 1. We see an increase in $\overline{k_{\mathrm{eff}}^{\mathrm{Mac(I)}}}$ of snow on all ice types until March 2020. After March $\overline{k_{\mathrm{eff}}^{\mathrm{Mac(I)}}}$ decreases. This is especially prominent on FYI and SYI areas.

The average R for the winter is lowest on leads and FYI areas, increasing slightly on SYI, and highest on ridged areas. R remained constant through the season on FYI and SYI. Leads and ridges had high variability between months.

4 Discussion

Before advancing our understanding of the snow's thermal conductivity heterogeneity and temporal trends, we must assess the performance of existing parametrizations on samples of snow measured on sea ice in the high Arctic. The microCT simulations allowed us to assess the current parametrizations for the complete ranges of density and anisotropy values. Following this, we introduced two new parametrizations, with and without anisotropy. When using these parametrizations to investigate the heterogeneity of the snow cover, the microCT was not an ideal method for obtaining a representative sampling of the snow cover due to the time required for one measurement. We, therefore, introduced the SMP to have a larger sampling density. The SMP does not have anisotropy measurements in parallel; therefore, a density parametrization ($k_{\mathrm{eff}}^{\mathrm{Mac(I)}}$, given in Equation (3)) was used for this up-scaling, as it had the highest r^2 value for this data set when compared to the $k_{\mathrm{eff}}^{\mathrm{FEM}}$ values. This approach ensured that the measured variability within the data set is a direct result of spatial and temporal variability, and imprecise parametrizations are not influencing the results. The implications of our findings are discussed below.

4.1 Assessing existing parametrizations

225 High-density variability of the sub-samples alongside a large spread of anisotropy values allowed us to create parametrizations of thermal conductivity (and test existing parametrizations) for all ranges of density (from 50 kg m^{-3} to 900 kg m^{-3}) and anisotropy (from 0.25 to 2). The relationship between density and $k_{\mathrm{eff}}^{\mathrm{FEM}}$ in Fig. 2 was compared to the parametrizations from Calonne et al. (2019) at -20 ^{o}C and Sturm et al. (1997). Through this comparison we can see that the anisotropy heavily influences the $k_{\mathrm{eff}}^{\mathrm{FEM}}$ values. A snow sub-sample with a density of 400 kg m^{-3} can have a thermal conductivity value ranging

230 from 0.2 W K^{-1}m^{-1} to 0.6 W K^{-1}m^{-1} if the snow is isotropic or anisotropic, respectively.

Comparing parametrizations of $k_{\mathrm{eff}}^{\mathrm{X}}$ and $k_{\mathrm{eff}}^{\mathrm{FEM}}$, seen in Fig. 4, allows us to analyze which parametrizations represent the simulated $k_{\mathrm{eff}}^{\mathrm{FEM}}$ most accurately. Fig. 4 shows that $k_{\mathrm{eff}}^{\mathrm{Yen}}$ and $k_{\mathrm{eff}}^{\mathrm{Stm}}$ work well for low effective thermal conductivity values. However, for the upper range of k_{eff} values, there is an underestimation when compared to $k_{\mathrm{eff}}^{\mathrm{FEM}}$. $k_{\mathrm{eff}}^{\mathrm{Cal3}}$, $k_{\mathrm{eff}}^{\mathrm{Cal20}}$, and $k_{\mathrm{eff}}^{\mathrm{Cal60}}$ appear to underestimate (overestimate) samples with high (low) anisotropy at lower $k_{\mathrm{eff}}^{\mathrm{FEM}}$ values. Despite this, $k_{\mathrm{eff}}^{\mathrm{Cal20}}$ has

235 a very similar r^2 value to the polynomial fit of this data set ($k_{\mathrm{eff}}^{\mathrm{Mac(I)}}$). The thermal conductivity of our samples at higher densities correspond to the Calonne et al. (2019) predictions at -20^oC; this is a result of our simulations using k_{ice} at -20^oC $= 2.34$ W K^{-1} m^{-1}. When introducing an anisotropy parameter, X = Löwe (Löwe et al., 2013) is well suited for low densities, below 500 kg m^{-3}, but start underestimating for sub-samples with densities higher than 500 kg m^{-3}. This was expected as the parametrization was not built for higher densities. We correct this parametrization for higher densities, resulting in the $k_{\mathrm{eff}}^{\mathrm{Mac(II)}}$

240 parametrization with an r^2 of 0.99.

In summary, we have introduced two new thermal conductivity parametrizations; see Equations (3) and (4). The latter requires an anisotropy factor, which can, for now, only be measured in the laboratory using microCT. We recommend using Equation (3) when measuring the thermal conductivity of snow on Arctic sea ice when only density measurements or approximations are available. $k_{\mathrm{eff}}^{\mathrm{Mac(I)}}$ is used throughout this study when there were no co-measured anisotropy values, for example,

245 when using the SMP. It is important to mention that calculations of $k_{\mathrm{eff}}^{\mathrm{FEM}}$ excludes convection.

4.2 Spatial variability

Due to the high heterogeneity of the snow cover on Arctic sea ice, the highly time-consuming microCT measurements could not represent the complete spatial variability. For this reason, we could up-scale using the SMP after analyzing suitable parametrizations from the microCT data set. As previously mentioned, the SMP does not have simultaneous anisotropy measurements,

250 so the parametrization $k_{\mathrm{eff}}^{\mathrm{Mac(I)}}$ was used. The SMP data set consisted of 3266 profiles taken during this study period. This is highly representative of the landscape due to the sheer number of measurements.

Grouping the data set by underlying ice type (FYI, SYI and leads) and topographic feature (ridges) allowed us to analyze different features of importance for heat transfer. Fig. 5 highlights that snow depth is highly dependent on the ridging of the ice, as known from other studies on sea ice ridging (Warren et al., 1999; Gradinger et al., 2010; Hames et al., 2022). ρ^{SMP} is

255 slightly higher for leads (likely due to the inclusion of brine in the snow on leads during formation, which lowers the freezing temperature and increases the density), and ridges (likely due to wind densification). However, the standard deviation is large

enough for these variations not to appear significant. $\overline{k_{\text{eff}}^{\text{Mac(I)}}}$ is derived from the ρ^{SMP}; therefore, we see similar dependencies in the groups, as explained above.

The average $k_{\text{eff}}^{\text{FEM}}$ for all sub-samples of this dataset had the value of 0.27 ± 0.17 W K^{-1} m^{-1} and the 1623 SMP profiles
260   harmonically averaged between January and March profiles of $\overline{k_{\text{eff}}^{\text{Mac(I)}}}$ had an average value of 0.25 ± 0.05 W K^{-1} m^{-1}, seen in Fig. 3. This compares to the constant average value of $\overline{k_{\text{eff}}^{\text{Models}}}$ (also represented as k_s) $= 0.30-0.33$ W K^{-1} m^{-1} proposed by Maykut and Untersteiner (1971) and Semtner Jr (1976). This snow thermal conductivity value is inferred from thermodynamic ice growth and is widely used in the modelling community (Sturm et al., 2002; Lecomte et al., 2013; Holland et al., 2021). We propose that large-scale sea ice models test a lower average k_s) value of 0.25 ± 0.05 W K^{-1} m^{-1} for snow
265   on sea ice. We have calculated this using independent methods. It is an open question what the influence of convection is, but we need to answer the question: what would happen in Arctic sea ice models if the established value of k_{eff} was too high?

The snowpack's thermal resistance R on sea ice heavily depends on topography. Ridged areas showed approximately three times the thermal resistance compared to level ice areas. SYI and FYI areas have similar R medians, with SYI areas having larger variability than FYI areas. Finally, leads have the lowest R and have a large standard deviation. Sampling bias is likely
270   one reason for these large standard deviations (especially on ridged and lead areas). Leads can not be measured until there is sufficient ice thickness to walk on. However, different ages and seasons produce highly varying conditions on the leads Clemens-Sewall et al. (2022), and our sampling was not focused on measuring different ages of leads throughout the season. This means that our sampling was likely not representative of the many different conditions of leads and cannot be used to draw concrete conclusions about snow thickness and thermal resistance. The high variability in the ridge's R values is due to the
275   highly varying snow distribution. SMP measurements were taken adjacent and perpendicular to the ridges to try and capture this variability.

In this data set, we have captured the spatial variability of the MOSAiC floe in contrast to thermal conductivity measured from thermistor strings installed in the snow and ice (Marchenko et al., 2019). Thermistor strings do not measure spatial variability of the thermal conductivity (only temporal) unless using an array set-up (Pringle et al., 2007). They are also destruc-
280   tive measurements and disturb the snow cover during installation. Therefore it is hard to capture the snow's effective thermal conductivity using this method.

4.3 Temporal change

The time component of this study shows that HS is highly variable, but the monthly median of SYI and lead areas appear to remain consistent throughout the season. FYI increased until March, thereafter showing a decrease. This decrease in snow
285   depth is likely due to the large wind speeds during the storm event described by Wagner et al. (2022). HS in ridged areas has high variability and is likely due to the blocks within the ridges causing an uneven sea ice topography causing high variability in snow accumulation. Temporal variability of the ridged sites could also be due to the operator selecting different areas of the ridge to measure or the sudden inaccessibility of different snowpit sites as a consequence of ice dynamics.

By conducting this analysis, we have seen that there is an increase of ρ^{SMP} on all ice types (and therefore also an increase of
290    $\overline{k_{\text{eff}}^{\text{Mac(I)}}}$) until March 2020, followed by a decrease in both ρ^{SMP} and $\overline{k_{\text{eff}}^{\text{Mac(I)}}}$. This seasonal trend in ρ^{SMP} can be seen in Fig. 5.

Fig. 6 confirms this seasonal trend by comparing multiple-density data sets. As snow undergoes metamorphism, we expect its thermal conductivity to increase as the density increases. However, an alternative process causing a density reduction is more dominant after March. We now work to understand the process causing a reduction in density after March. The air temperature at 2 meters, the downward shortwave (SW) radiation and the wind speed is plotted in Fig. 6. After March, we see an increase

295   in SW radiation and two warm air intrusions in April. Wind speed's variability remains high from November to May. Taking the atmospheric conditions into account, this density reduction and reduction in penetration force at the surface in Fig. 7 could result from:

– Fresh snowfall as input would lower the average density. A layer with low thermal conductivity $\overline{k_{\mathrm{eff}}^{\mathrm{Mac(I)}}}$ leads to a drastic decrease in the average thermal conductivity. We can see in Wagner et al. (2022) that we had fresh snowfall during this

300   period.

The reduction in penetration force at the lower depths could be a combined effect of the below three points:

– Erosion of the snow surface as a result of high wind speeds. Wagner et al. (2022) showed a reduction in SWE during this period and concluded that this was driven by the erosion of the snow. Erosion of the surface snow would leave behind a less dense lower snowpack, resulting in an overall reduction in density. This process would also explain the reduction in

305   snow depth.

– Vapour diffusion within the snowpack and sublimation of the snow surface produces a density reduction at the bottom. Jafari et al. (2020)'s simulations showed significant density reductions upon including diffusive water vapour transport within SNOWPACK. They showed that diffusive vapour transport could result in cumulative density changes of -62 to -66 kg m^{-3} for the bottom layer in a shallow Arctic snowpack and snow on sea ice. More work on implementing

310   SNOWPACK with vapour diffusion and studying this period would be required to confirm if this is a dominant process causing a density reduction.

– Penetration of the hard density layers at the snow-ice interface (named the 'remnant surface scattering layer' in Section 3.1) became thinner due to sublimation, contributing less to the overall statistics of high densities at the interface. A reduction in measured densities at the lower depths would also reduce the SMP-derived SWE. Therefore, this would also

315   apply to the transect analysis in Wagner et al. (2022). More work investigating this snow-ice interface layer is required to form a conclusion.

Implementing a higher-density upper layer and lower-density lower layer into models should be essential. Crocus and SNOWPACK simulate lower layers with high density and high thermal conductivity, and surface layers with low values for both variables (Domine et al., 2019), whereas we have presented the opposite. Further modelling work needs to be undertaken

320   to determine these processes' contributions to the reduction in density, but this is beyond the scope of this study.

Due to the combination of this seasonal trend in density and $\overline{k_{\mathrm{eff}}^{\mathrm{Mac(I)}}}$ snow depths, we see no change of R on level ice, with a value of $R = 515 \pm 404$ m^2 K W^{-1} on first-year ice and 660 ± 475 m^2 K W^{-1} on second-year ice. We can therefore conclude

that the calculated values of R remain consistent during the winter period but include high spatial heterogeneity due to snow depth variability. Ridged areas show a high variability throughout the season but no significant change in the average R from January to May.

5 Conclusions

Using measurements of snow microstructure on different ice types and topographic features on Arctic sea ice for a seven-month winter period in the high Arctic, we have evaluated for the first time the seasonal evolution and spatial heterogeneity of the snow's thermal conductivity and thermal resistance. We assessed the current thermal conductivity parametrizations and their performance for the complete range of possible snow and firn densities. We present two new parametrizations, with and without anisotropy.

Field measurements highlighted the need for a high sampling density to represent spatial heterogeneity of thermal conductivity due to snow's high heterogeneity in the Arctic sea ice system. We conclude that the SMP data set used in this study can be used to measure the thermal conductivity's heterogeneity as it had a large sampling size. However excluding anisotropy and convection are limitations of this approach. We propose testing lower values of snow thermal conductivities in large-scale sea ice models. The average of $\overline{k_{\mathrm{eff}}^{\mathrm{Mac(I)}}}$ in this study was $0.25 \pm 0.05 \,\mathrm{W\,K^{-1}\,m^{-1}}$ for snow on sea ice. This indicates that $0.32 \pm 0.01 \,\mathrm{W\,K^{-1}\,m^{-1}}$, currently used in sea ice modelling, largely overestimates thermal conductivity.

By studying the temporal variability, we infer and quantify from three independent density measurements an increase in the snow's density up to March and a decrease after that. It was found that a combination of fresh snowfall, high wind speeds causing erosion and re-deposition (initiating a SWE reduction during a storm event, as shown in Wagner et al. (2022)), vapour diffusion within the snow and changes at the snow-ice interface (further analysis of this interface is needed to draw concrete conclusions. However, this is not in the scope of this study), could all result in the density reduction across the snow profile. This density trend projected the thermal conductivity on first-year and second-year ice before the melt period started. Since a similar non-monotonic behaviour is extracted for the snow depth, the thermal resistance of snow on level sea ice remains approximately constant with a value of $R = 515 \pm 404 \,\mathrm{m^2\,K\,W^{-1}}$ on first-year ice and $660 \pm 475 \,\mathrm{m^2\,K\,W^{-1}}$ on second-year ice. Although the $\overline{k_{\mathrm{eff}}^{\mathrm{Mac(I)}}}$ on ridged areas did not vary significantly in comparison to level areas, we found approximately three times higher thermal resistance on ridges ($1411 \pm 910 \,\mathrm{m^2\,K\,W^{-1}}$), with extremely high spatial heterogeneity due to snow depth. We conclude that ridged and level areas need to be treated separately in modelling, as thermal resistance is almost three times higher in ridged areas. High spatial variability of thermal resistance is apparent but temporal changes in the snow cover are minimal during this period.

6 Data availability

All snow datasets used in this article are published in Pangaea. The snowpit raw data is publicly available from: https://doi.org/10.1594/PANGAEA.935934. This data set includes SMP, microCT, density cutter and SWE data sets.

Shortwave radiation measurements were obtained from the Atmospheric Radiation Measurement (ARM) User Facility, a U.S. Department of Energy (DOE) Office of Science User Facility Managed by the Biological and Environmental Research Program, and are publicly available in the ARM data archive (Riihimaki, 2021).

Near-surface meteorology (2-meter air temperature and wind speed) and surface energy flux measurements from the University of Colorado/ NOAA surface flux team are available through the Arctic Data Center (Cox et al., 2021).

7 Author contributions

A.R.M: Data curation, Investigation, Visualization, Formal analysis, Writing (original draft, review and editing). H.L: Conceptualisation, Formal analysis, Writing (review and editing). L.G: Visualization, Formal analysis, Writing (review and editing). D.N.W: Data curation, Investigation, Writing (review and editing). R.D: Data curation, Investigation, Writing (review and editing). R.O: Formal analysis, Writing (review and editing). M.S: Project administration, Funding acquisition, Conceptualisation, Methodology, Investigation, Writing (review and editing).

8 Competing interests

The authors declare that they have no known competing interests.

9 Acknowledgements

Data sets used in this manuscript were produced as part of the international Multidisciplinary drifting Observatory for the Study of the Arctic Climate (MOSAiC) with the tag MOSAiC20192020 and the Project_ID: AWI_PS122_00. We thank all people involved in the expedition of the Research Vessel Polarstern (Knust, 2017) during MOSAiC in 2019–2020 as listed in Nixdorf et al. (2021). We want to thank Scanco Medical AG for lending and supporting the use of the MicroCT90 throughout the MOSAiC expedition.

10 Funding

Swiss Polar Institute (SPI reference DIRCR-2018-003) Funder ID: http://dx.doi.org/10.13039/501100015594. European Union's Horizon 2020 research and innovation program projects ARICE (grant 730965) for berth fees associated with the participation of the DEARice project. WSL Institute for Snow and Avalanche Research SLF. WSL_201812N1678. Funder ID: http://dx.doi.org/10.13039/501100015742.

References

Arndt, S.: Sensitivity of sea ice growth to snow properties in opposing regions of the Weddell Sea in late summer, Geophysical Research
380   Letters, 49, e2022GL099 653, 2022.

Arns, C. H., Knackstedt, M. A., Pinczewski, M. V., and Lindquist, W.: Accurate estimation of transport properties from microtomographic
images, Geophysical research letters, 28, 3361–3364, 2001.

Bergman, T. L., Bergman, T. L., Incropera, F. P., Dewitt, D. P., and Lavine, A. S.: Fundamentals of heat and mass transfer, John Wiley &
Sons, 2011.

385 Blunier, T. and Schwander, J.: Gas enclosure in ice: age difference and fractionation, in: Physics of Ice Core Records, pp. 307–326, Hokkaido
University Press, 2000.

Calonne, N., Flin, F., Morin, S., Lesaffre, B., du Roscoat, S. R., and Geindreau, C.: Numerical and experimental investigations of the effective
thermal conductivity of snow, Geophysical research letters, 38, 2011.

Calonne, N., Milliancourt, L., Burr, A., Philip, A., Martin, C. L., Flin, F., and Geindreau, C.: Thermal Conductivity of Snow, Firn, and Porous
390   Ice From 3-D Image-Based Computations, Geophysical Research Letters, 46, 13 079–13 089, 2019.

Clemens-Sewall, D., Smith, M. M., Holland, M. M., Polashenski, C., and Perovich, D.: Snow redistribution onto young sea ice: Observations
and implications for climate models, Elem Sci Anth, 10, 00 115, 2022.

Cox, C., Gallagher, M., Shupe, M., Persson, O., Solomon, A., Blomquist, B., Brooks, I., Costa, D., Gottas, D., Hutchings, J., et al.: 10-
meter (m) meteorological flux tower measurements (Level 1 Raw), Multidisciplinary drifting observatory for the study of arctic climate
395   (MOSAiC), central Arctic, October 2019–September 2020, Arctic Data Center. DOI: http://dx. doi. org/10.18739/A2VM42Z5F, 2021.

Domine, F., Bock, J., Morin, S., and Giraud, G.: Linking the effective thermal conductivity of snow to its shear strength and density, Journal
of Geophysical Research: Earth Surface, 116, 2011.

Domine, F., Barrere, M., and Sarrazin, D.: Seasonal evolution of the effective thermal conductivity of the snow and the soil in high Arctic
herb tundra at Bylot Island, Canada, The Cryosphere, 10, 2573–2588, 2016.

400 Domine, F., Picard, G., Morin, S., Barrere, M., Madore, J.-B., and Langlois, A.: Major issues in simulating some Arctic snowpack properties
using current detailed snow physics models: Consequences for the thermal regime and water budget of permafrost, Journal of Advances
in Modeling Earth Systems, 11, 34–44, 2019.

Eicken, H., Fischer, H., and Lemke, P.: Effects of the snow cover on Antarctic sea ice and potential modulation of its response to climate
change, Annals of Glaciology, 21, 369–376, 1995.

405 Fichefet, T. and Maqueda, M. M.: Sensitivity of a global sea ice model to the treatment of ice thermodynamics and dynamics, Journal of
Geophysical Research: Oceans, 102, 12 609–12 646, 1997.

Fukusako, S.: Thermophysical properties of ice, snow, and sea ice, International Journal of Thermophysics, 11, 353–372, 1990.

Garboczi, E. J. et al.: Finite element and finite difference programs for computing the linear electric and elastic properties of digital images
of random materials, 1998.

410 Gouttevin, I., Langer, M., Löwe, H., Boike, J., Proksch, M., and Schneebeli, M.: Observation and modelling of snow at a polygonal tundra
permafrost site: spatial variability and thermal implications, The Cryosphere, 12, 3693–3717, https://doi.org/10.5194/tc-12-3693-2018,
publisher: Copernicus Publications, 2018.

Gradinger, R., Bluhm, B., and Iken, K.: Arctic sea-ice ridges—Safe heavens for sea-ice fauna during periods of extreme ice melt?, Deep Sea
Research Part II: Topical Studies in Oceanography, 57, 86–95, 2010.

415 Hames, O., Jafari, M., Wagner, D. N., Raphael, I., Clemens-Sewall, D., Polashenski, C., Shupe, M. D., Schneebeli, M., and Lehning, M.: Modeling the small-scale deposition of snow onto structured Arctic sea ice during a MOSAiC storm using snowBedFoam 1.0., Geoscientific Model Development, 15, 6429–6449, 2022.

Holland, M. M., Clemens-Sewall, D., Landrum, L., Light, B., Perovich, D., Polashenski, C., Smith, M., and Webster, M.: The influence of snow on sea ice as assessed from simulations of CESM2, The Cryosphere, 15, 4981–4998, 2021.

420 Huwald, H., Tremblay, L.-B., and Blatter, H.: Reconciling different observational data sets from Surface Heat Budget of the Arctic Ocean (SHEBA) for model validation purposes, Journal of Geophysical Research: Oceans, 110, 2005.

Jafari, M., Gouttevin, I., Couttet, M., Wever, N., Michel, A., Sharma, V., Rossmann, L., Maass, N., Nicolaus, M., and Lehning, M.: The impact of diffusive water vapor transport on snow profiles in deep and shallow snow covers and on sea ice, Frontiers in Earth Science, 8, 249, 2020.

425 Kaempfer, T. U., Schneebeli, M., and Sokratov, S.: A microstructural approach to model heat transfer in snow, Geophysical Research Letters, 32, 2005.

King, J., Howell, S., Brady, M., Toose, P., Derksen, C., Haas, C., and Beckers, J.: Local-scale variability of snow density on Arctic sea ice, The Cryosphere, 14, 4323–4339, 2020.

Knust, R.: Polar research and supply vessel POLARSTERN operated by the Alfred-Wegener-Institute, Journal of large-scale research facili-
430 ties JLSRF, 3, A119–A119, 2017.

Lecomte, O., Fichefet, T., Vancoppenolle, M., Domine, F., Massonnet, F., Mathiot, P., Morin, S., and Barriat, P.-Y.: On the formulation of snow thermal conductivity in large-scale sea ice models, Journal of Advances in Modeling Earth Systems, 5, 542–557, https://doi.org/10.1002/jame.20039, 2013.

Löwe, H., Riche, F., and Schneebeli, M.: A general treatment of snow microstructure exemplified by an improved relation for thermal
435 conductivity, The Cryosphere, 7, 1473–1480, 2013.

Macfarlane, A. R., Schneebeli, M., Dadic, R., Wagner, D. N., Arndt, S., Clemens-Sewall, D., Hämmerle, S., Hannula, H.-R., Jaggi, M., Kolabutin, N., Krampe, D., Lehning, M., Matero, I., Nicolaus, M., Oggier, M., Pirazzini, R., Polashenski, C., Raphael, I., Regnery, J., Shimanchuck, E., Smith, M. M., and Tavri, A.: Snowpit SnowMicroPen (SMP) force profiles collected during the MOSAiC expedition, PANGAEA, https://doi.org/10.1594/PANGAEA.935554, in: Macfarlane, AR et al. (2021): Snowpit raw data collected during the MOSAiC
440 expedition. PANGAEA, https://doi.org/10.1594/PANGAEA.935934, 2021a.

Macfarlane, A. R., Schneebeli, M., Dadic, R., Wagner, D. N., Arndt, S., Clemens-Sewall, D., Hämmerle, S., Hannula, H.-R., Jaggi, M., Kolabutin, N., Krampe, D., Lehning, M., Matero, I., Nicolaus, M., Oggier, M., Pirazzini, R., Polashenski, C., Raphael, I., Regnery, J., Shimanchuck, E., Smith, M. M., and Tavri, A.: Snowpit raw data collected during the MOSAiC expedition, https://doi.org/10.1594/PANGAEA.935934, 2021b.

445 Marchenko, S., Cheng, G., Lötstedt, P., Pohjola, V., Pettersson, R., Van Pelt, W., and Reijmer, C.: Thermal conductivity of firn at Lomonosov-fonna, Svalbard, derived from subsurface temperature measurements, The Cryosphere, 13, 1843–1859, 2019.

Maykut, G. A. and Untersteiner, N.: Some results from a time-dependent thermodynamic model of sea ice, Journal of Geophysical Research, 76, 1550–1575, 1971.

Mellor, M.: Engineering properties of snow, Journal of Glaciology, 19, 15–66, 1977.

450 Nicolaus, M., Perovich, D. K., Spreen, G., Granskog, M. A., von Albedyll, L., Angelopoulos, M., Anhaus, P., Arndt, S., Belter, H. J., Bessonov, V., et al.: Overview of the MOSAiC expedition: Snow and sea ice, 2022.

Nixdorf, U., Dethloff, K., Rex, M., Shupe, M., Sommerfeld, A., Perovich, D. K., Nicolaus, M., Heuzé, C., Rabe, B., Loose, B., et al.: MOSAiC extended acknowledgement, 2021.

Orvig, S.: Climates of the polar regions, Elsevier Pub. Co., 1970.

455 Perovich, D. K. et al.: The optical properties of sea ice, 1996.

Petrasch, J., Schrader, B., Wyss, P., and Steinfeld, A.: Tomography-based determination of the effective thermal conductivity of fluid-saturated reticulate porous ceramics, Journal of heat transfer, 130, 2008.

Pitman, D. and Zuckerman, B.: Effective thermal conductivity of snow at $-88°$, $-27°$, and $-5°$ C, Journal of Applied Physics, 38, 2698–2699, 1967.

460 Pringle, D., Eicken, H., Trodahl, H., and Backstrom, L.: Thermal conductivity of landfast Antarctic and Arctic sea ice, Journal of Geophysical Research: Oceans, 112, 2007.

Radionov, V. F., Bryazgin, N. N., and Alexandrov, E. I.: The Snow Cover of the Arctic Basin., Tech. rep., WASHINGTON UNIV SEATTLE APPLIED PHYSICS LAB, 1997.

Riche, F. and Schneebeli, M.: Microstructural change around a needle probe to measure thermal conductivity of snow, Journal of Glaciology,
465 56, 871–876, 2010.

Riche, F. and Schneebeli, M.: Thermal conductivity of snow measured by three independent methods and anisotropy considerations, The Cryosphere, 7, 217–227, 2013.

Riihimaki, L.: Radiation instruments on Ice (ICERADRIIHIMAKI), Atmospheric Radiation Measurement (ARM) user facility. DOI: http://dx. doi. org/10.5439/1608608, 2021.

470 Semtner Jr, A. J.: A model for the thermodynamic growth of sea ice in numerical investigations of climate, Journal of Physical Oceanography, 6, 379–389, 1976.

Singh, A.: An investigation of the thermal conductivity of snow, Journal of Glaciology, 45, 346–351, 1999.

Slack, G. A.: Thermal conductivity of ice, Physical Review B, 22, 3065, 1980.

Smith, M. and Jamieson, B.: A new set of thermal conductivity measurements, in: Proceedings of the International Snow Science Workshop,
475 pp. 507–510, 2014.

Sturm, M. and Johnson, J. B.: Thermal conductivity measurements of depth hoar, Journal of Geophysical Research: Solid Earth, 97, 2129–2139, 1992.

Sturm, M. and Massom, R. A.: Snow in the sea ice system: Friend or foe, Sea ice, pp. 65–109, 2017.

Sturm, M., Holmgren, J., König, M., and Morris, K.: The thermal conductivity of seasonal snow, Journal of Glaciology, 43, 26–41, 1997.

480 Sturm, M., Holmgren, J., and Perovich, D. K.: Winter snow cover on the sea ice of the Arctic Ocean at the Surface Heat Budget of the Arctic Ocean (SHEBA): Temporal evolution and spatial variability, Journal of Geophysical Research: Oceans, 107, SHE–23, 2002.

Wagner, D. N., Shupe, M. D., Cox, C., Persson, O. G., Uttal, T., Frey, M. M., Kirchgaessner, A., Schneebeli, M., Jaggi, M., Macfarlane, A. R., et al.: Snowfall and snow accumulation during the MOSAiC winter and spring seasons, Cryosphere, 16, 2373–2402, 2022.

Warren, S. G., Rigor, I. G., Untersteiner, N., Radionov, V. F., Bryazgin, N. N., Aleksandrov, Y. I., and Colony, R.: Snow depth on Arctic sea
485 ice, Journal of Climate, 12, 1814–1829, 1999.

West, A., Collins, M., and Blockley, E.: Using Arctic ice mass balance buoys for evaluation of modelled ice energy fluxes, Geoscientific Model Development, 13, 4845–4868, 2020.

Yen, Y.-C.: Review of thermal properties of snow, ice, and sea ice, vol. 81, US Army, Corps of Engineers, Cold Regions Research and Engineering Laboratory, 1981.

490   Yen, Y.-C., Cheng, K., and Fukusako, S.: A review of intrinsic thermophysical properties of snow, ice, sea ice, and frost, The Northern Engineer, 24, 53–74, 1991.